Chapter 2
Linear and Nonlinear Optical Properties of Some Tellurium Oxide Glasses

Cid B. de Araújo and Luciana R.P. Kassab

2.1 Introduction

A large number of heavy-metal oxide (HMO) glasses doped with rare-earth (RE) ions has been studied by several decades and still attracting interest from the basic point of view as well as for applications in lasers, amplifiers, displays, modulators, switches, optical limiters, and sensors, among other applications. Indeed, a variety of HMO glasses (e.g., tellurites [1], germanates [2, 3], and antimony [2, 4]) still deserves numerous studies motivated by their large transmittance from the visible to the near-infrared, small phonon energies, large chemical stability, large acceptance of RE ions doping, and high nonlinear (NL) optical response. These characteristics allowed the successful use of HMO glasses for studies performed by many groups (see, e.g., refs. [1, 2, 5, 6]).

Among the HMO used for photonics, the tellurium oxide glasses (TOG) show several advantages when compared with other glasses. Beside the facile methods of fabrication of bulk TOG samples, these glasses are particularly important because of their thermal, mechanical, and chemical properties that allow processing the glass to fabricate films of good optical quality, synthesizing glass-ceramics, and manufacturing optical fibers and rectangular waveguides. In general, TOG present linear refractive indices of ≈2, large transmittance window (360–1000 nm), low cutoff phonon energy (≈700/cm), large mechanical resistance, high chemical durability, high vitreous stability, and high solubility of RE ions doping species.

C.B. de Araújo (✉)
Departamento de Física, Universidade Federal de Pernambuco, 50670-901 Recife, PE, Brazil
e-mail: cid@df.ufpe.br

L.R.P. Kassab
Faculdade de Tecnologia de São Paulo/CEETEPS, 01124-060 São Paulo, SP, Brazil

V.A.G. Rivera, D. Manzani (eds.), *Technological Advances in Tellurite Glasses*,
Springer Series in Materials Science 254, DOI 10.1007/978-3-319-53038-3_2

In this chapter, we review some of our previous results obtained with samples having different TOG compositions. In Sect. 2.2, we will describe the methods used for the sample's fabrication and their basic characterization. In Sect. 2.3, we describe studies related to the phenomena of Stokes and anti-Stokes photoluminescence (PL) in TOG pure and doped with RE. Also samples containing silver nanoparticles (Ag-NPs) or silicon nanocrystals (Si-NCs) were studied, and some results are reviewed. In Sect. 2.4, we report NL optical experiments where the NL refraction and NL absorption of TOG samples were measured aiming their evaluation for application in all-optical devices. Finally, in Sect. 2.5, a summary of the results and further comments on the potential of TOG for photonics are given.

2.2 Methods Used for Fabrication and Characterization of the TeO_2-Based Glasses

The samples used were prepared by the conventional melt-quenching technique. All reagents and doping species were oxide powders obtained commercially. The high pure reagents (~99.999%) were melted in platinum crucibles, at different temperatures (750–800 °C) depending on the composition, during 20–120 min, quenched in air, in a heated brass mold, annealed for 2 h at 270–360 °C to avoid internal stress, and then cooled to room temperature inside the furnace. After cooling, the glass samples were cut and polished for the optical experiments. For the experiments with glasses having Ag-NPs, the samples with compositions including $AgNO_3$ were submitted to additional heat treatment (HT), at the annealing temperature, during different periods of time, to reduce the Ag^+ ions to Ag^0 and to nucleate Ag-NPs; samples without Ag-NPs were also produced to be used for comparison with the samples having NPs. The samples doped with RE ions containing Si-NCs were also prepared by the melt-quenching method, and more details of their fabrication are given in Sect. 2.3.3. In all PL experiments, we observed that the emitted intensities do not change after HT of the samples without $AgNO_3$ (or without Si-NCs), but they change as a function of the Ag-NPs (or -Si-NCs) amount that was controlled by the HT duration in the samples containing $AgNO_3$ (or Si-NCs).

To determine the size and shape of the Ag-NPs and Si-NCs, a high-resolution transmission electron microscope (HR-TEM) operating at 300 kV was used. A spectrophotometer that operates in the visible and near-infrared regions was used to measure the absorption spectra of the samples from 300 to 1000 nm, and the linear refractive index was measured using the M-line technique.

PL spectra were measured with different excitation sources, depending on the doping species and the goals of each experiment. For continuous-wave (CW) excitation in the visible range, a xenon lamp coupled to a 0.25 m monochromator was used. For excitation in the infrared, the light sources used were CW diode lasers operating either at 980 nm or 805 nm. The PL signals obtained with the CW sources

were analyzed by a phase fluorometer equipped with a 0.25 m spectrometer coupled to a CCD. For the experiments with pulsed lasers, two sources were used. An optical parametric oscillator (400 kW, pulses of 5 ns, repetition rate of 20 Hz) pumped by a Q-switched Nd:YAG laser was used for the PL studies with basis on phonon-assisted transitions. In these experiments, the signals were recorded using photomultipliers coupled to digital oscilloscopes and computers. For the NL optical experiments, a Q-switched and mode-locked laser (1064 nm, 17 ps, 10 Hz) was used. The experiments were based on the Z-scan technique integrated in a 4f-system, as described in [7, 8]. The image receiver at the output of the 4f-system is a 1000 × 1018 pixels cooled CCD camera (−30 °C) operating with a fixed gain. The sample is moved in the focal region along the beam propagation direction (Z axis). *Open-* and *closed-aperture* Z-scan normalized transmittances are numerically processed from the acquired images by integrating over all the pixels in the first case and over a circular numerical filter in the second one (corresponding to a linear aperture transmittance S = 0.73 in order to optimize simultaneously the sensitivity and the signal-to-noise ratio). The incident intensity was adjusted by a polarizing system at the entry of the setup.

A Ti:sapphire laser (800 nm, 1.56 eV, 76 MHz, 150 fs) was used for measurements based on the Kerr gate technique [9]. The laser beam was split in two beams: probe and pump beams with intensities of 508 MW/cm^2 and 52 MW/cm^2, respectively. The sample was positioned between two crossed polarizers. The probe beam propagates along the Z axis, and the pump beam propagates along a direction forming a small angle ($\approx 1^\circ$) with the Z axis. The angle between the electric fields of the pump and probe beams was set to 45°. When the pulses of the two beams overlap spatially and temporally on the sample, the pump beam induces an NL birefringence, and the polarization of the probe beam rotates while propagating through the sample. Then, a fraction of the probe beam is transmitted through a polarizer/analyzer, which is oriented perpendicularly to the electric field of the incident probe beam. The signal, collected by a photodiode, is analyzed as a function of the delay time between the pump and probe pulses.

Most of the experiments were performed at room temperature, but in the case of Sect. 2.3.1, the sample's temperature was varied from 100 to 540 K.

2.3 Stokes and Anti-Stokes Photoluminescence

The PL experiments were performed using samples with various compositions having different trivalent RE ions. The main goal was the investigation of the contribution of phonon transitions in a TOG sample (Sect. 2.3.1) and the contribution of the Ag-NPs (Sect. 2.3.2) and Si-NCs (Sect. 2.3.3) for the PL enhancement.

2.3.1 *Frequency Upconversion Assisted by Phonon Annihilation*

Frequency upconversion (UC) is a phenomenon in which PL with wavelength smaller than the excitation wavelength is emitted by a physical system. The UC process is also referred as anti-Stokes PL, while the emission with wavelength longer than the excitation wavelength is called Stokes PL. The UC process finds many applications, such as infrared-pumped compact lasers operating in the visible range [10], infrared-to-visible converters and light harvesting, important for solar cells [11], temperature sensors [12], and colored displays [13], among others. Normally, UC is a NL process in which two or more photons from the excitation beam are absorbed to generate one UC photon. Changing the sample's temperature is an interesting possibility for controlling the UC spectrum exploiting phonon-assisted transitions in RE-doped materials. The experiment reviewed in this section was performed to investigate a thermally activated UC emission in an Nd^{3+}-doped TeO_2-ZnO glass (labeled as TZO glass), prepared with 2.0 wt% of Nd_2O_3 according to the procedure summarized in Sect. 2.2 and described in details in ref. [14]. The sample was studied by resonant excitation of the Nd^{3+} transition $^4I_{9/2} \rightarrow {}^4F_{5/2}$ at 805 nm. Figure 2.1a, b shows the room temperature PL spectrum from 340 to 800 nm. The UC emission centered at 754 nm, due to transition $^4F_{7/2} \rightarrow {}^4I_{9/2}$, presented linear intensity dependence versus the laser intensity and exhibited 670-fold enhancement when the sample's temperature changed from 200 K to 535 K; this is the largest value reported for thermally assisted one-photon-induced UC emission. The other emissions, associated to other electronic transitions, show NL dependence with the laser intensity. They were identified in comparison with previous measurements in various Nd^{3+}-doped glasses [14]. Figure 2.2a, b illustrates the behavior of the emission at 754 nm versus the laser intensity and temperature. The slope in Fig. 2.2a indicates that only one laser photon at 805 nm is involved in the generation of each 754 nm UC photon. Considering the excitation

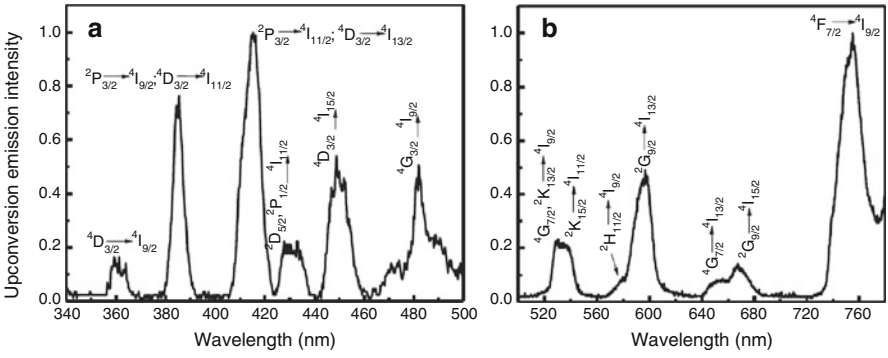

Fig. 2.1 Room temperature UC emission spectrum of Nd^{3+}-doped TeO_2-ZnO glass for pulsed excitation at 850 nm [14]. The bands amplitudes were normalized to the bands at 415 nm (**a**) and 754 nm (**b**)

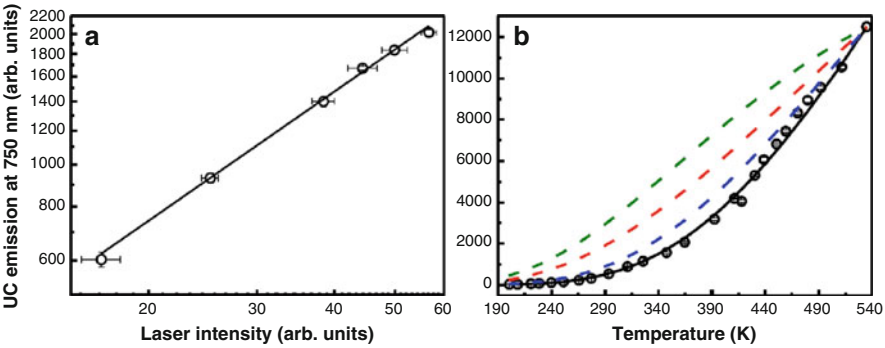

Fig. 2.2 (**a**) Dependence of the UC intensity at 754 nm versus the laser intensity at room temperature. (**b**) Comparison between the experimental data (*circles*) and the model results for different temperatures (EPM = 700/cm, *black solid line*; EPM = 400/cm, *green dashed line*; EPM = 850/cm, *red dashed line*; and EPM = 600/cm, *blue dashed line*) [14]

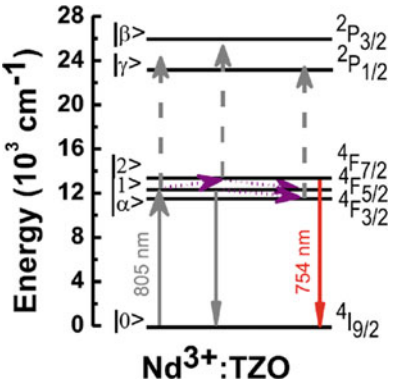

Fig. 2.3 Simplified energy levels scheme of Nd^{3+} representing the pathway to generate UC emission at 754 nm by excitation at 805 nm. Solid (*dashed lines*) upward arrows represent laser excitation from the fundamental (excited) level; dotted lines represent phonon-assisted temperature-dependent process, and the downward arrows represent radiative transitions. The fundamental and excited states are represented by |0>, |1>, and |2>, respectively [14]

conditions and the linear behavior of the UC emission versus the laser intensity, we may conclude that the signal is originated in a process which starts with the resonant absorption $^4I_{9/2} \rightarrow {}^4F_{5/2}$ followed by annihilation of phonons with promotion of the excited ions to the thermally coupled $^4F_{7/2}$ level from where the PL at 754 nm originates. This UC pathway was verified measuring the temperature dependence of the PL intensity. Figure 2.2b shows the 670-fold PL enhancement related to the temperature change from 200 K to 535 K. A rate-equation model for Nd^{3+} population densities based on the levels scheme of Fig. 2.3, including temperature-dependent absorption cross sections and nonradiative transition rates, describes the thermal behavior of the UC process. The temperature dependence of the one-photon-excited UC emission is well described considering the so-called

effective phonon mode (EPM) [15], with energy of 700/cm, illustrated in Fig. 2.3b by the black solid line that shows a good match with the experimental data. The numerical results considering other different EPM values, 400/cm (green dashed lines), 850/cm (red dashed lines), and 600/cm (blue dashed lines), are also shown.

From the results shown in Fig. 2.2b, we concluded that it is not the matrix cutoff phonon mode the one dominating the phonon-assisted UC transition but the EPM, which represents a statistical average that takes into account the phonon's energies and their occupation phonon number [15]. We recall that the observation of the phonon-assisted UC phenomenon in a fluoroindate glass [16] revealed a large sensitivity to the sample's conditions such as humidity and mechanical resistance. Normally, TOG, either in bulk or as optical fibers, are much more stable than fluoroindate glasses; for the TZO glass, the reproducibility of the results is less affected by the external conditions than fluoroindate glasses. Another important point to be considered is the fact that the UC process reported for TZO requires only one EPM and then it is more efficient than the previously reported cases that require participation of multiphonon transitions.

2.3.2 *Enhanced Frequency Upconversion and Energy Transfer in the Presence of Metallic Nanoparticles*

PL enhancement in rare-earth (RE)-doped HMO glasses containing metallic NPs has been investigated by many authors after the pioneer paper by Malta et al. [17]. The influence of the NPs on the PL efficiency of the RE ions is larger when the incident light and/or the PL wavelengths are near resonant with the resonance frequency of the localized surface plasmons (LSP), the quanta of coherent free-electron oscillations in the NPs. The NPs' dielectric function, their shape and size distribution, the host environment, and the relative distances between the ions and the NPs are important parameters that influence the PL efficiency. PL quenching due to ET from the RE ion to the NP is dominant when the distance NP-RE ion is small [18].

The influence of metal NPs on the PL of glasses with various compositions was also studied by various groups (see, e.g., [19–25]).

One successful way to grow silver or gold NPs inside HMO glasses is based on the melt-quenching method. The appropriate concentration of NPs and their average size and shapes depend on the glass viscosity, and the growth process is controlled by the diffusion of the metal atoms and ions in the melt that also depends on the procedure used for the heat treatment. Therefore, one important step to obtain large PL enhancement is the efficient nucleation of the metallic NPs through controlled HT of the samples. The selection of materials with appropriate parameters is a hard task when one is performing experiments with NPs ensembles such as the ones performed with glasses. Also, the selection of glasses with large transparency window and small cutoff phonon energy is very important to reduce the

probability of nonradiative relaxation of the RE ions. As mentioned in the previous sections, TGO glasses are excellent materials for PL experiments because they present chemical and physical characteristics that contribute for the fabrication of good samples. In all cases studied by us, the presence of NPs contributed for the PL efficiency either due to the influence of the large local field on the RE ions positioned in the vicinity of the NPs or due to the energy transfer (ET) from the NPs to the RE ions. PL quenching was observed when the NPs concentration was above certain values because the proximity between the RE ions and the NPs increases the probability of ET from the excited RE ions to the NPs.

We demonstrated the nucleation of metallic NPs in various TOG compositions [21, 26–35] containing Ag-NPs and Au-NPs. The presence of Pb^{2+} clusters in TeO_2-PbO-GeO_2 glasses with Ag-NPs led to enhanced PL in the visible range [28], whereas for Pr^{3+}-doped TeO_2-PbO-GeO_2 glass, enhanced Stokes and anti-Stokes emission were successfully observed and analyzed [21, 29]. Further experiments with TeO_2-PbO-GeO_2 glass doped with Eu^{3+} and containing Au-NPs [30] and Tb^{3+}-doped TeO_2-ZnO-Na_2O-PbO glass with Ag-NPs [31] were also reported. In all cases, large increase in the samples' luminescence was observed. The role of ET processes was also exploited in TOG containing metallic NPs and co-doped with two different RE species.

Some selected examples of our work with tellurium oxide-based glasses are described below:

2.3.2.1 Tb^{3+}/Eu^{3+}-Co-Doped TZNP Glasses with Ag-NPs

The first PL study on the influence of Ag-NPs in Tb^{3+}/Eu^{3+}-co-doped TeO_2-ZnO-Na_2O-PbO glasses (labeled as TZNP glasses) was reported in [32]. The samples were prepared with 2.0 wt% of Tb_4O_7, 1.0 wt% of Eu_2O_3, and 4.0 wt% of $AgNO_3$. In the experiments, the samples were excited using light with frequency larger than the frequency bandgap of the glass, at 355 nm, which is possibly in resonance with Tb^{3+} and Eu^{3+} transitions originating from the ground state. However, absorption by Ag-NPs may also occur. Luminescence bands from 480 to 700 nm were observed due to radiative transitions associated to Eu^{3+} and Tb^{3+}. The contribution of ET processes and the intensified local field due to the Ag-NPs allowed obtaining enhanced PL in the orange-red spectral region.

Figure 2.4 shows the absorption spectra of the samples from 350 to 700 nm. Transitions originating from the ion ground state are observed at 480 nm (Tb^{3+}: $^7F_6 \rightarrow D_4$), 465 nm (Eu^{3+}: $^7F_0 \rightarrow {}^5D_2$), and 395 nm ($Eu^{3+}$: $^7F_0 \rightarrow {}^5L_6$). The broadband centered at ≈490 nm, observed in the samples heat-treated for times longer than 2 h, is attributed to LSP resonances. The absorption band presents an inhomogeneous broadening due to the various shapes and sizes of Ag-NPs as well as aggregates in the samples. The band amplitude increases for longer HT times due to the increase of the Ag-NPs' volume fraction.

PL measurements were performed using a 15 W xenon lamp (pulses of 3 μs at 80 Hz), followed by a 0.2 m monochromator to select the wavelength at 355 nm.

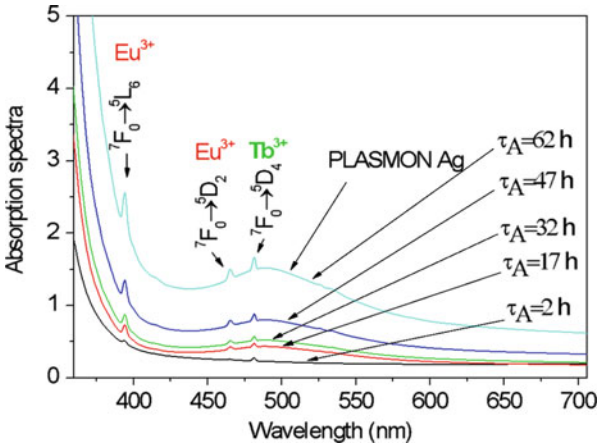

Fig. 2.4 Absorption spectra in Tb^{3+}/Eu^{3+}-doped TZNP glasses with Ag-NPs, heat-treated during various times [36]

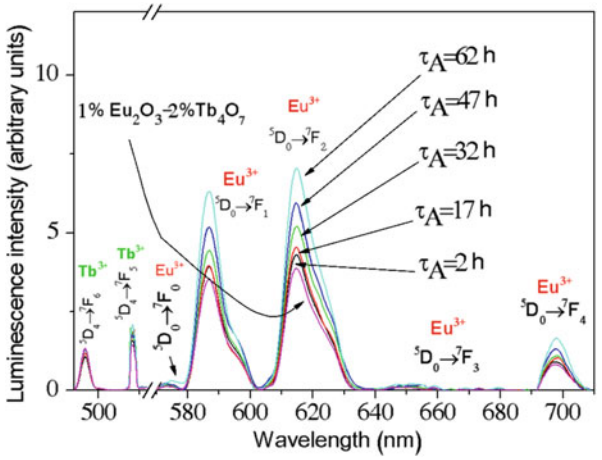

Fig. 2.5 PL spectra in in Tb^{3+}/Eu^{3+}-doped TZNP glasses with Ag-NPs for HT during different times; the results for the sample without Ag-NPs are shown for reference (excitation at 355 nm) [32]

The luminescence spectra in Fig. 2.5 exhibit bands due to 4f-4f transitions associated to Tb^{3+} and Eu^{3+}. The results for different HT times show that the PL intensity in the orange-red region is enhanced while increasing the volume fraction occupied by the NPs. No PL signal in this spectral range was detected when the samples containing only Eu^{3+} were excited under the same conditions. So the simultaneous presence of Tb^{3+} and Eu^{3+} is essential to observe the strong PL signal in the orange-red region; the emissions originating from the Eu^{3+} levels grow with the increase of the HT time reaching an enhancement of ~100%. As can be observed comparing Figs. 2.4 and 2.5, the LSP band overlaps with the $^5D_0$ level, and then an increase in the Eu^{3+} luminescence is expected due to the enhanced local field in the proximity of the NPs. As the excitation wavelength is not in resonance with the LSP absorption band, ET from excited Ag-NPs to the RE may occur, but it is not the dominant process. The spectra of Fig. 2.5 can be understood by analyzing the Tb^{3+}/Eu^{3+} energy level scheme shown in Fig. 2.6.

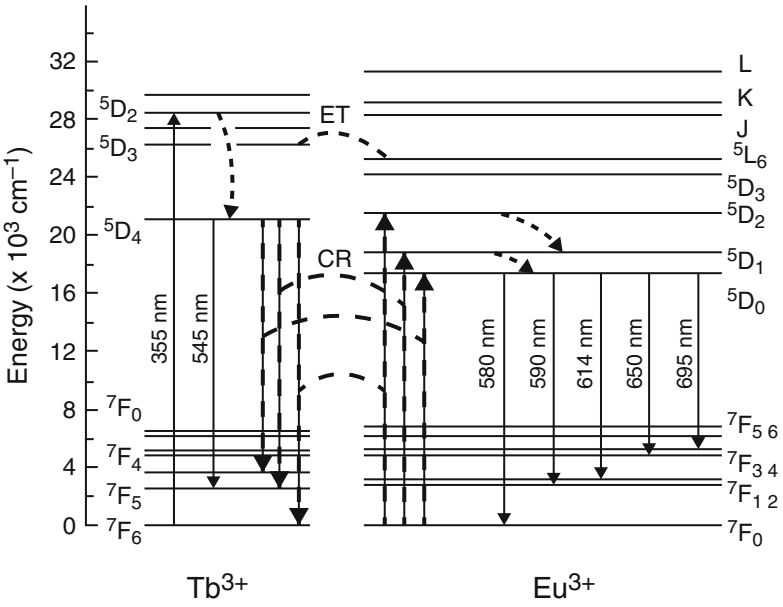

Fig. 2.6 Energy levels scheme of Tb^{3+} and Eu^{3+}. The *solid lines* represent radiative transitions, and *dotted lines* represent phonon relaxation process. *Dashed lines* represent CR and ET processes [32]

One possible UC pathway is due to ET from the $^5D_3$ (Tb^{+3}) level to the energy level $^5L_6$ (Eu^{3+}); from this level, after nonradiative relaxation, the Eu^{3+} excitation reaches level $^5D_0$ from where radiative transitions to Eu^{3+} levels ^7F_j (J = 0–4) may occur. Another energy pathway starts with nonradiative relaxation from level $^5D_3$ (Tb^{3+}) to $^5D_4$ (Tb^{3+}) providing radiative relaxations from $^5D_4$ (Tb^{3+}) to the Tb^{3+} levels ^7F_j (J = 0–6) related to emissions in the blue-red spectral region. Also quasi-resonant cross-relaxation (CR) to Eu^{3+} levels ^5D_j (J = 0, 1, 2) may occur, as indicated in Fig. 2.6. Efficient CR processes are very probable considering the large concentration of RE ions. Following the CR, radiative decay corresponding to Eu^{3+} transitions $^5D_0 \rightarrow {}^7F_J$ (J = 0–4) takes place. We note that the Tb^{3+} emissions at 485 and 545 nm are weak because of the ET to Eu^{3+}.

Figure 2.7 summarizes the relative increase of the luminescence bands at 590 and 614 nm as a function of the HT time. The results indicate that a large number of Eu^{3+} are properly located nearby the Ag-NPs. There is always an ideal distance that favors enhancement of the PL, and if some ions are not in adequate positions, this may be the cause for not obtaining a large PL enhancement. In the present case, the contribution of ET processes and the intensified local field due to the Ag-NPs allowed obtaining enhanced PL in the orange-red spectral region, but unfortunately the method of sample fabrication does not allow control of the relative RE-NP distance.

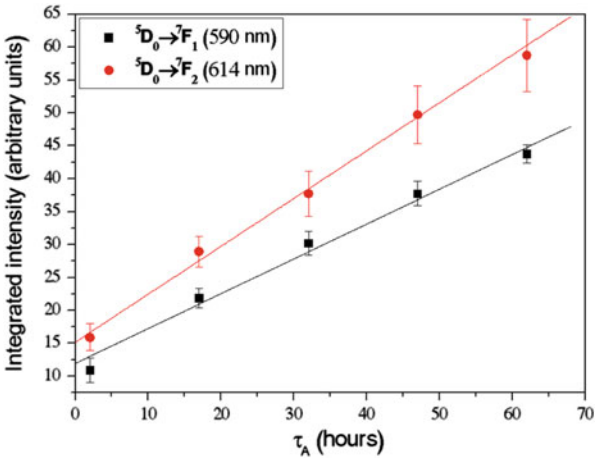

Fig. 2.7 Integrated PL intensity for the Eu^{3+} transitions at 590 nm and 614 nm versus the HT time [32]

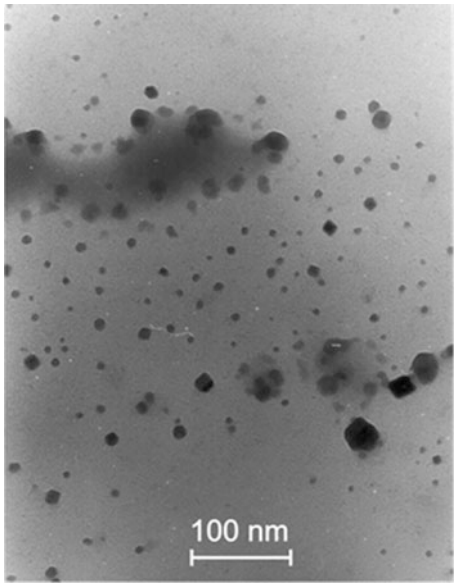

Fig. 2.8 TEM image of the Tm^{3+}-doped TZO glass containing Ag-NPs, heat-treated during 48 h [33]

2.3.2.2 Tm^{3+}-Doped TZO Glass with Ag-NPs

Infrared-to-visible and infrared-to-infrared UC processes in Tm^{3+}-doped TZO glass containing Ag-NPs were studied in another TGO glass with large potential for photonic applications [33]. The choice of Tm^{3+} was motivated by the large infrared-to-visible UC efficiency reported for other TGO glassy hosts and due to the several applications already demonstrated for Tm^{3+}-doped glasses. In the present case, the doping species were 0.5 Tm_2O_3 and 2.0 $AgNO_3$ (in wt%). One TEM image of the samples studied is shown in Fig. 2.8 for the sample heat-treated during

48 h at 325 °C. Isolated Ag-NPs with diameters from ≈10 nm to ≈50 nm and aggregates with various shapes can be seen. Figures 2.9 and 2.10, obtained with excitation at 1050 nm, show that the PL bands centered in ≈477 nm, ≈650 nm, and ≈800 nm, corresponding to the transitions $^1G_4 \rightarrow {}^3H_6$, $^1G_4 \rightarrow {}^3F_4$, and $^3H_4 \rightarrow {}^3H_6$, respectively, change their amplitude for different HT times. Notice that all PL bands increase with the HT up to 48 h. One order of magnitude enhancement is observed for the whole PL spectra that is a remarkable result in comparison with our previous reports for other RE ions [21, 29–32]. The spectra corresponding to HT during 72 h show a partial quenching of the PL intensity. Again the results can be understood recalling that heat treating the samples for very long time leads to large Ag-NPs concentration and the relative distances between the Tm^{3+} and the NPs become very small. Then the excited Tm^{3+} transfer the energy absorbed from the

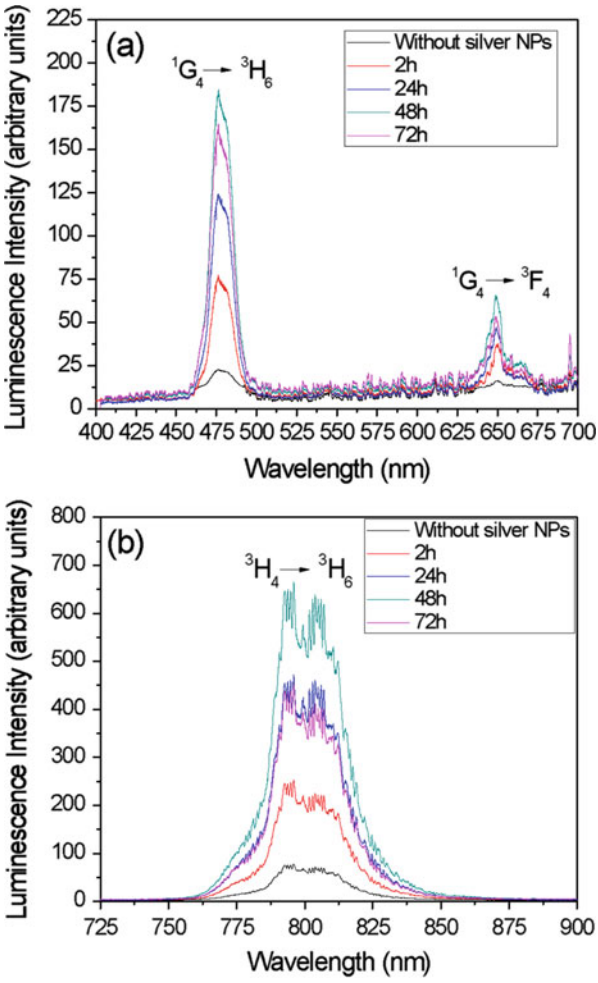

Fig. 2.9 Emission spectra of Tm^{3+}-doped TZO glass containing Ag-NPs, for different HT times. Excitation at 1050 nm [33] (**a**) visible luminescence (**b**) near-infrared luminescence

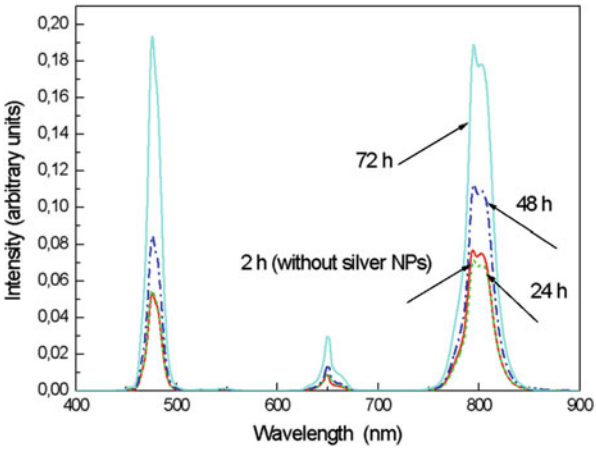

Fig. 2.10 Emission spectra of Tm^{3+}/Yb^{3+}-doped TZO glass containing Ag-NPs, for different HT times. Excitation at 980 nm [26]

laser beam to the NPs which dissipate the energy by heat. The dependence of the UC signals with the laser intensity was analyzed to identify the possible routes corresponding to each UC emission. Log-log plots of the UC intensities versus the laser intensity for the transitions $^2G_4 \rightarrow {}^3H_6$, $^1G_4 \rightarrow {}^3F_4$, and $^3H_4 \rightarrow {}^3H_6$ present slopes of ≈2.7, ≈2.8, and ≈1.8, respectively, indicating that the PL bands at 477 nm and 650 nm are due to the absorption of three laser photons, while the transition $^3H_4 \rightarrow {}^3H_6$ is due to the absorption of two photons. The UC processes occur because of the intermediate phonon-assisted steps. Even the excited state absorption $^3F_4 \rightarrow {}^3F_{2,3}$ which is resonant is followed by emission of phonons due to the decay from level $^3F_{2,3}$ to the level $^3H_4$.

The present results demonstrate the large influence of Ag-NPs in the infrared-to-visible and infrared-to-infrared UC luminescence of Tm^{3+}-doped TZO glasses. Enhancement of the UC emission in the heat-treated samples is attributed to the increase of the local field on the Tm^{3+} located in the vicinity of the NPs as the frequency of the incident light beam is not close to the LSP resonance frequency of the Ag-NPs. The tenfold enhancement observed for the whole PL spectrum is an important result that illustrates the potential of using metal-dielectric composites to improve the performance of luminescent materials containing RE ions.

2.3.2.3 Tm^{3+}/Yb^{3+}-Doped TZO with Ag-NPs

For several years, Tm^{3+}-doped TGO glasses have attracted PL studies because there are metastable levels of Tm^{3+} suitable for UC luminescence in the blue and green spectral region. Addition of Yb^{3+} enhances the efficiency of infrared-to-visible conversion due to the large ET rate from excited Yb^{3+} to Tm^{3+}. However, although efficient infrared-to-visible conversion was obtained for Yb^{3+}/Tm^{3+}-co-

doped materials [37, 38], obtaining larger UC enhancement is still of great interest. The results presented in this section show the possibility of finding new approaches to reach larger UC enhancement by nucleation of Ag-NPs inside of a Yb^{3+}/Tm^{3+} TGO nanocomposite prepared with 0.5 wt% of Tm_2O_3, 3.0 wt% of Yb_2O_3, and 4.0 wt% of $AgNO_3$. The HT procedure described in Sect. 2.2 was used for the Ag-NPs nucleation during various time intervals. PL bands corresponding to Tm^{3+} transitions were observed at 480 nm, 650 nm, and 800 nm due to the ET from Yb^{3+} to Tm^{3+}, by excitation with a diode laser operating at 980 nm, in resonance with the Yb^{3+} transition $^2F_{7/2} \rightarrow {}^2F_{5/2}$. UC emissions centered at 480 nm, 650 nm, and 800 nm, due to the Tm^{3+} transitions ($^1G_4 \rightarrow {}^3H_6$, $^1G_4 \rightarrow {}^3F_4$, and $^3H_4 \rightarrow {}^3H_6$), were measured, and large enhancement (≈300%) for the UC luminescence was observed in the heat-treated samples in comparison with samples without Ag-NPs as shown in Fig. 2.10. As in the cases presented before, the growth of the PL bands correlates with the increase of the volume fraction occupied by the Ag-NPs. TEM images obtained for the samples heat-treated during 24 and 72 h are shown in Fig. 2.11. Particles with average diameters varying from 30 nm (for the sample heat-treated during 24 h) to 10 nm (sample heat-treated during 72 h) were observed together

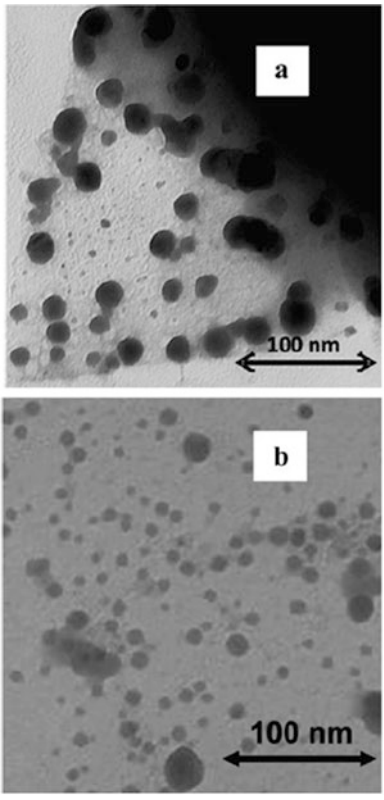

Fig. 2.11 TEM image of the Tm^{3+}/Yb^{3+}-doped TZO glass containing Ag-NPs, for HT during 24 h (**a**) and 72 h (**b**) [26]

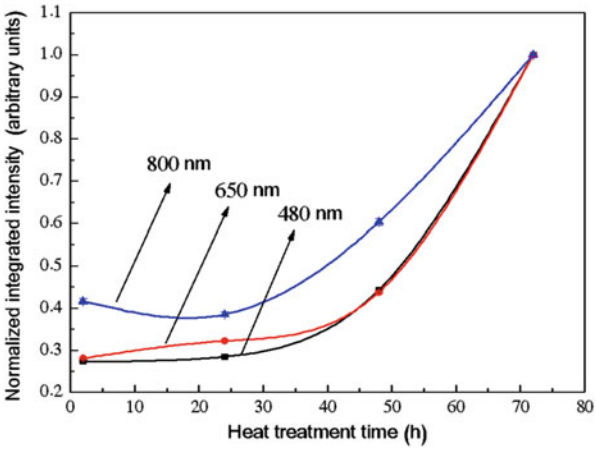

Fig. 2.12 Normalized integrated intensity of Tm^{3+}/Yb^{3+}-doped TZO glass containing Ag-NPs [26]

with aggregates of NPs with dimensions of ≈80 nm nm that can also be seen. This result shows that longer HT produces fragmentation of the large particles and aggregates formed during the initial 24 h period; the growth of the PL bands correlates with the increase of the Ag-NPs concentration. The integrated intensity of the each PL band shown in Fig. 2.12 grows considerably for increasing HT times, and the bands at 480 and 650 nm, having wavelengths near the LSP resonances of the isolated NPs, present larger derivative as a function of the HT time. The PL band at 800 nm is also enhanced due to the presence of aggregates. The large PL enhancement of the Tm^{3+} transitions is attributed to the resonance of the laser wavelength with the Yb^{3+} transition that is more intense than the 4f-4f transitions of Tm^{3+} and the Yb^{3+} concentration that is six times larger than the Tm^{3+} concentration. The quadratic dependence of the PL band centered at 800 nm, corresponding to the transition $^3H_4 \rightarrow {}^3H_6$, with the laser power shown in Fig. 2.13, indicates that two excited Yb^{3+} participate in the generation process transferring their energies to one Tm^{3+}. The transitions $^1G_4 \rightarrow {}^3H_6$ (480 nm) and $^1G_4 \rightarrow {}^3F_4$ (650 nm) present slopes equal to ≈3 indicating that three excited Yb^{3+} are participating in the UC process. The PL growth due to the HT of the samples demonstrates that Ag-NPs play an essential role in the UC processes that involve triads and quartets of the RE ions. The radiative transitions corresponding to visible light, close to resonance with the LSP, are more influenced by the isolated NPs. A comparison between the present results and the results for Yb^{3+}/Tm^{3+}-doped germanate glasses [39] shows larger UC enhancement for the TZO glass even for a three-time smaller amount of silver in the starting glass composition but with a more appropriate concentration ratio between Tm^{3+} and Yb^{3+}.

These results represented the first report showing the PL enhancement in the presence of silver nanostructures involving triads and quartets of RE ions in a TGO nanocomposite.

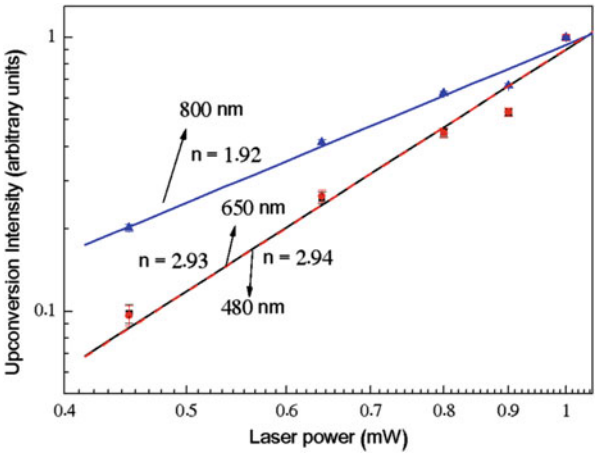

Fig. 2.13 UC intensity as a function of the laser power for Tm^{3+}/Yb^{3+}-doped TZO glass containing Ag-NPs [26]

2.3.2.4 Er^{3+}-Doped TWB Glasses with Ag-NPs

Experiments performed with Er^{3+}-doped TeO_2-WO_3-Bi_2O_3 glasses (labeled as TWB glasses) illustrate well the contribution of Ag-NPs to increase the PL efficiency of TGO glasses doped with RE ions [34]. The effect of the NPs on the Er^{3+} luminescence was controlled by appropriate HT of the samples prepared with 1.0 wt% of Er_2O_3 and 2.0 wt% of $AgNO_3$. Enhancement up to 700% was obtained for the upconverted emissions at 527 nm, 550 nm, and 660 nm, when the sample excitation is made at 980 nm. Since the laser frequency is far from the NPs' LSP resonance frequency, the PL enhancement was attributed to the local field increase in the proximity of the NPs and not to ET from the NPs to the emitters. This was the first time that the effect was investigated for tellurite-tungstate-bismutate glasses, and the enhancement observed is the largest reported for a TGO glass. Figure 2.14 shows a TEM image of a sample heat-treated during 24 h, with Ag-NPs having an average size of 35 nm; the electron diffraction pattern in the inset of Fig. 2.14 shows the crystalline structure of the NPs. The LSP absorption band is not clearly observed in the spectra of Fig. 2.15 because of the small amount of Ag-NPs and the strong absorption of the TWB glasses in the blue region and because large NPs present broadband resonances with small amplitudes. However, the spectra reveal the contribution of the LSP absorption band as a tail in the blue-green region. The LSP resonance wavelength is estimated to be between 420 and 500 nm considering the dielectric function of silver [40] and the glass refractive index (~2), in agreement with the tail observed in Fig. 2.15.

Figure 2.16 shows the UC spectra of the samples. The PL bands centered at 527 nm, 550 nm, and 660 nm correspond to the $^2H_{11/2} \rightarrow {}^4I_{15/2}$, $^4S_{3/2} \rightarrow {}^4I_{15/2}$, and $^4F_{9/2} \rightarrow {}^4I_{15/2}$ transitions of Er^{3+}, respectively. Notice that the largest enhancement of the emission at 550 nm was obtained for HT during 24 h, whereas for 48 h and 72 h, the UC signal is reduced, probably because the concentration of Ag-NPs became large and then the average distance NP-RE ion became smaller than the

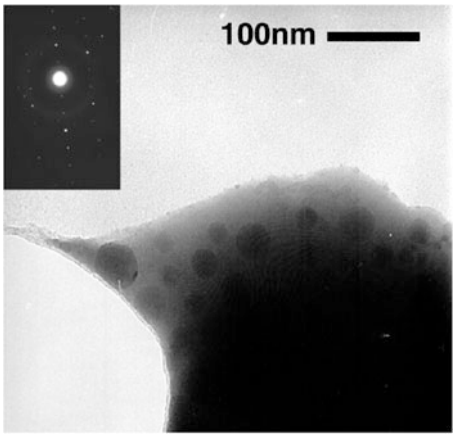

Fig. 2.14 Transmission electron microscope image of Er^{3+}-doped TWB glass with Ag-NPs heat-treated during 24 h [34]

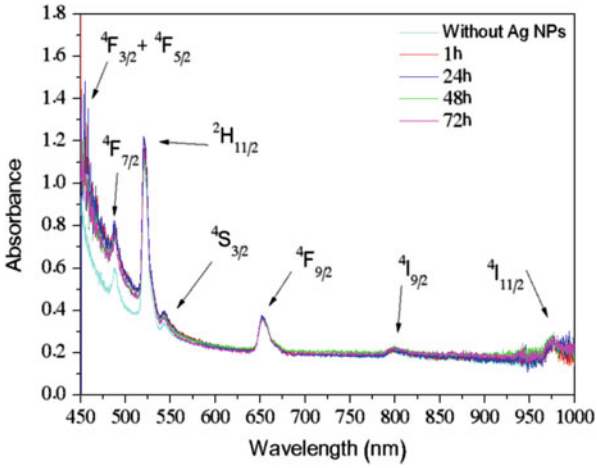

Fig. 2.15 Absorption spectra of Er^{3+}-doped TWB glass heat-treated during various time intervals. The spectrum of a sample without Ag-NPs is also shown for comparison with the other samples [34]

optimum distance for PL enhancement. Again, since the 980 nm excitation wavelength is far from the LSP resonance wavelength, the probability of direct excitation of the LSP band is small, and ET from the NPs to the Er^{3+} is negligible. So the intensity enhancement observed is attributed to the increased local field in the vicinities of the Ag-NPs. The quadratic dependence of the UC intensities versus the laser intensity, shown in Fig. 2.17, indicates that two laser photons are contributing to generate each UC photon. The excitation pathway is the same identified in previous experiments with lead germanate glasses corresponding to two steps of one-photon absorption, according to $^4I_{15/2} \rightarrow {}^4I_{13/2} \rightarrow {}^4F_{7/2}$ [41]. The same intensity behavior was observed for the other samples.

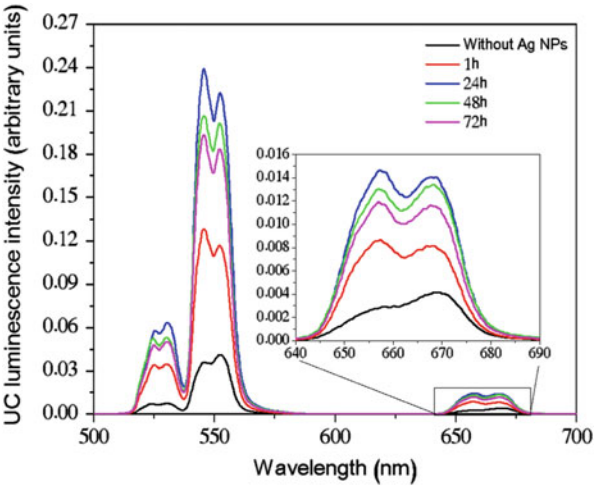

Fig. 2.16 UC luminescence spectra of Er^{3+}-doped TZO glasses heat-treated during various time intervals; the spectrum of the sample without Ag-NPs is also shown for comparison with the other samples [34]

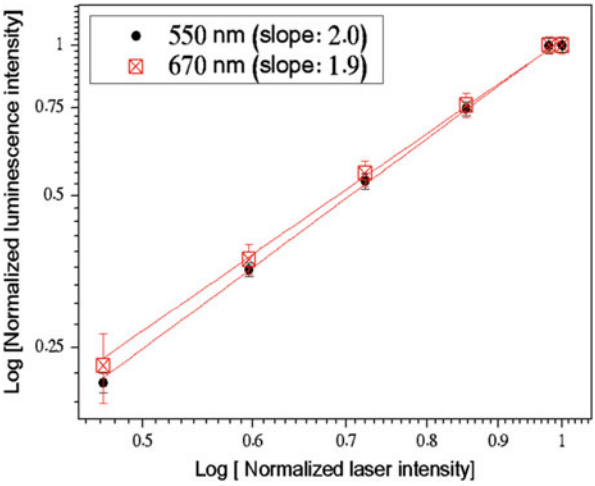

Fig. 2.17 Dependence of the UC signals at 550 and 660 nm versus the laser intensity for the sample heat-treated during 24 h [34]

2.3.3 Rare-Earth Photoluminescence in the Presence of Silicon Nanocrystals

Another way to obtain PL enhancement of RE ions has been demonstrated using semiconductor nanocrystals (NCs) [36, 42–51]. The absorption cross sections of the NCs are usually larger than the RE cross sections, and then ET from the NCs to the RE ions may be an efficient mechanism to achieve growth of the RE luminescence. In this case, the size of the NCs may be adjusted to match their energy gap and the energy of the desired RE emitting states.

In this section, we review recent results of the enhanced PL in TZO glass doped with Er^{3+} and containing Si-NCs. This was the first study of a TGO glass in which the nucleation of Si-NCs was obtained using the melting-quenching technique. The previous reports of enhanced Er^{3+} luminescence were based on silicate glass containing Si-NCs prepared by more complex techniques such as ion implantation, lithography, or chemical vapor deposition [43, 48–53]. For TZO glasses doped with Er^{3+} and containing different concentration of Si-NCs, the PL increase was attributed to ET from excited Si-NCs to the Er^{3+} located in the vicinity of the NCs. In this case the samples were prepared with 1.0% of Er_2O_3 and different concentrations of silicon powder (0.01, 0.1, and 0.4 wt%). Enhancement of ≈300% was observed in the visible and in the near-infrared regions. In particular, the fourfold enhancement observed for the broad emission centered at ≈1530 nm, corresponding to the Er^{3+} transition $^4I_{3/2} \rightarrow {}^4I_{15/2}$, indicates large potential of the composite material for interface with existing telecommunication devices. Figure 2.18a–d shows TEM images of Si-NCs with average sizes of 20 nm and 50 nm, obtained with melting temperatures of 800 °C and 900 °C, respectively. Figure 2.19a, b shows the PL spectra of the samples melted at 800 °C, while Fig. 2.19c, d shows the results for the samples melted at 900 °C (PL spectra for samples without Si-NCs are also shown for comparison). The bands observed correspond to the transitions $^2H_{11/2} \rightarrow {}^4I_{15/2}$ (≈525 nm), $^4S_{3/2} \rightarrow {}^4I_{15/2}$ (≈545 nm), $^4F_{9/2} \rightarrow {}^4I_{15/2}$ (≈680 nm), and $^4I_{13/2} \rightarrow {}^4I_{15/2}$ (≈1530 nm). The signals at 545 nm and 1530 nm are enhanced by ≈200% for the

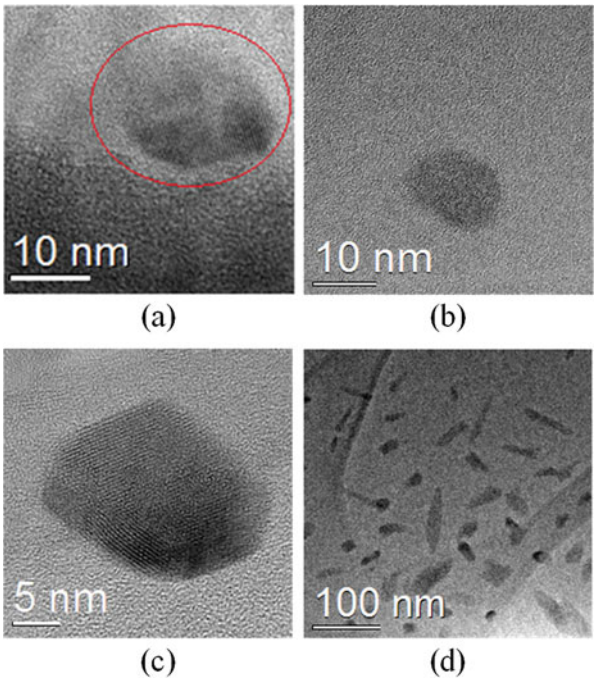

Fig. 2.18 Electron microscope images of Si-NCs in Er^{3+}-doped TZO glasses. (**a**) and (**b**), 0.1 wt% and 0.4 wt% Si samples melted at 800 °C; (**c**) and (**d**), 0.4 wt% Si sample melted at 900 °C [35]

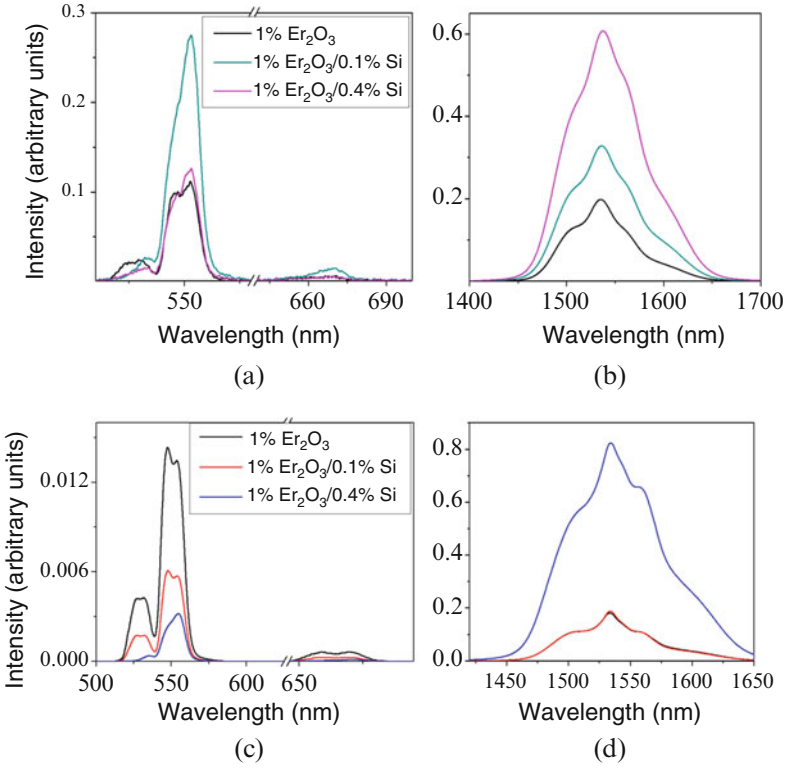

Fig. 2.19 Infrared-to-visible frequency UC and downconversion in Er^{3+}-doped TZO glass with Si-NCs (excitation wavelength: 980 nm). (a) and (b), samples melted at 800 °C; (c) and (d), samples melted at 900 °C [35]

samples melted at 800 °C, in comparison with the samples without Si-NCs. In the samples prepared with 0.4 wt% of Si powder and melted at 900 °C, PL quenching of the visible emission and large enhancement of ≈300% for the 1530 nm emission are observed. These results show that the Si-NCs play an important role on the PL behavior of the samples. The PL quenching in the visible range, attributed to the process of back ET from excited Er^{3+} to the Si-NCs, is larger in the samples with higher Si concentration as well as in the samples with the larger Si-NCs sizes. This result together with the larger enhancement observed in the sample melted at 900 °C is due to the higher absorption cross section of the larger Si-NCs and also indicates that more Er^{3+} are located in the vicinities of the Si-NCs than in the samples melted at 800 °C.

A study of the PL intensity versus the laser intensity for the signals at 545 nm and 1530 nm, emitted by the samples melted at 800 °C and 900 °C, was performed and showed quadratic (linear) dependence of the PL intensity at 545 nm (at 1530 nm) versus the laser intensity indicating that two laser photons generate one photon in the visible range, while only one laser photon is involved in the

generation of each photon at 1530 nm. These processes are similar to the ones observed in [54] for germanate glasses. Because the large Si-NCs have indirect bandgap, the electron-hole recombination rate is small, and then the ET process from the Si-NCs to Er^{3+} is favored. The PL enhancement in the green range is attributed to the interaction between two excited Si-NCs and one Er^{3+}, while the enhancement of the emission at 1530 nm is due to ET from one excited Si-NC to one Er^{3+}. The simple technique described here to embbed Si-NCs inside TGO glasses opens new routes for further studies. While in the case of metal NPs, large losses may occur due to the heating produced by the electron oscillations, in the case of Si-NCs this process is not relevant. However, the studies of PL enhancement of RE ions in TGO glasses are starting, and a deeper knowledge of all the processes involved in the samples preparation and control of the Si-NCs sizes and shapes are still necessary in order to explore this new route for obtaining more efficient PL enhancement.

2.4 Third-Order Nonlinear Optical Properties

Beside the large applicability of TOG for UC, these glasses are promising materials for infrared technologies, laser devices, and NL photonics. Their NL properties were studied by various authors who reported NL refractive index $n_2 \sim 10^{-15}$ cm^2/W and NL absorption coefficient $\alpha_2 \sim 10^{-1}$ cm/GW in the near-infrared [55–61]. The large nonlinearity of TOG is due to the high polarizability of the Te-O bonds and the electron lone pair of the Te^{2+} ion [62, 63]. The NL susceptibility of TOG may be enhanced by including in the glass composition compounds containing ions with lone pairs such as Bi^{3+} and Pb^{2+} or ions with unoccupied *d* orbitals such as W^{6+} or Nb^{5+}. From the results reported in the literature, it is clear that addition of Bi_2O_3 or Nb_2O_5 contributes to increase the value of n_2. However, in many cases, an increase of α_2 is also observed because of the optical bandgap reduction and/or introduction of new localized states inside the bandgap due to the non-bridging oxygen ion content. The increase in the α_2 value makes the glass composition not attractive for all-optical switching.

In this section, we review the third-order NL properties of a multicomponent TOG with composition in mol %, (80−x) TeO_2-15GeO_2-5K_2O-xBi_2O_3 for x = 5 (sample TGKB5), x = 10 (sample TGKB10), and x = 15 (sample TGKB15), at 800 nm and 1064 nm. The different amounts of TeO_2 and Bi_2O_3 were used to investigate their relative contribution for the nonlinearity. The samples were prepared by melting the raw materials, tellurium oxide (TeO_2), germanium oxide (GeO_2), bismuth oxide (Bi_2O_3), and potassium carbonate (K_2CO_3), previously stoichiometrically weighted in order to obtain 7 g of bulk glass. The starting powdered materials were mixed and loaded in a gold crucible. Then, the batch was melted at 760 °C for 1 h to ensure the complete elimination of CO_2 from the decomposition of the carbonate and a good homogenization and fining. Finally, the melt was cooled inside a stainless mold preheated at 20 °C below the glass

transition temperature, T_g , annealed at this temperature for 2 h and slowly cooled down to room temperature to minimize residual internal stress. The values of T_g and the crystallization temperature, T_x, for the three samples are given in [64].

The glass compositions investigated were previously used to fabricate microstructured optical fibers as well as co-doped optical fibers for white light generation and IR emission [65, 66].

Table 2.1 presents the linear refractive index, n_0, and linear absorption coefficient, α_0, of the samples studied. The values of n_0, α_0, and the optical bandgap, Eg, do not change much when the relative concentration of TeO_2 and Bi_2O_3 is changed. The large value of $n_0 \approx 2$ is due to the contribution of the electron lone pairs of Te^{2+} and Bi^{3+} and to their large polarizability.

As mentioned in Sect. 2.2, the NL refractive indices were measured using the Z-scan integrated in a 4f-system technique [7, 8]. Figure 2.20 shows the Z-scan profiles for the *closed-aperture* experiments indicating positive n_2 values for the three samples. The *open-aperture* Z-scan experiment exhibited a small NL absorption signal only for the TGB5 sample. For the other samples, the signal was smaller than the minimum value that our setup could detect (0.003 cm/GW).

The results obtained for n_2, summarized in Table 2.2 for the three samples, do not differ much because the hyperpolarizabilities of TeO_2 and Bi_2O_3 have the same order of magnitude. The large hyperpolarizability of TeO_2 is due to the empty $5d$ orbitals and to the electron lone pair of the Te^{2+} ion; Bi_2O_3 also contributes for the NL susceptibility by analogous reasons.

Table 2.1 Index of refraction, n_0, absorption coefficient, α_0, and optical bandgap, E_g

	n_0			α_0 (cm^{-1})		
Sample	800 nm	1064 nm	1550 nm	800 nm	1064 nm	E_g (eV)
TGKB5	2.10	2.08	2.02	0.11	0.13	3.16
TGKB10	2.12	2.10	2.03	0.12	0.11	3.08
TGKB15	2.14	2.11	2.04	0.11	0.14	3.06

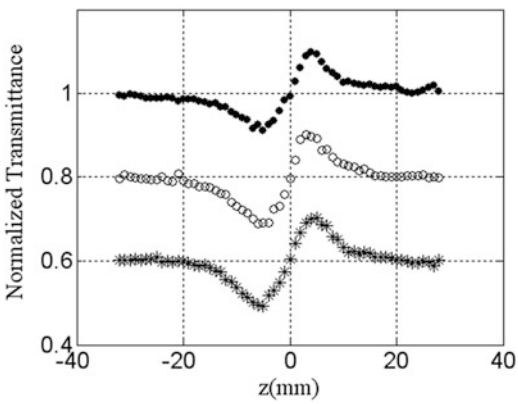

Fig. 2.20 Closed-aperture Z-scan profiles for excitation at 1064 nm. Laser intensity: 7 GW/cm^2 (sample TGKB5), 3 GW/cm^2 (sample TGKB10), 2.9 GW/cm^2 (sample TGKB15) [64]

Table 2.2 Nonlinear refractive indices of the samples

	$n_2(\times 10^{-16} cm^2/W)$	
Sample	800 nm	1064 nm
TGKB5	6.5 ± 0.7	46.5 ± 11.2
TGKB10	8.0 ± 0.8	56.3 ± 9.0
TGKB15	7.1 ± 0.7	48.8 ± 8.8

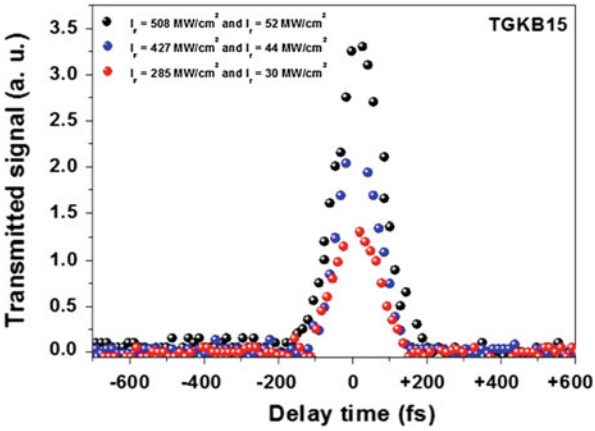

Fig. 2.21 Kerr gate signal at 800 nm for different probe intensities (sample TGKB15). Pump intensity: 508 MW/cm^2 [64]

The NL response at 800 nm is illustrated by Fig. 2.21 which shows the behavior of the Kerr gate signal as a function of the delay time between the pump and probe pulses. The setup for this experiment is described in Sect. 2.2.

The symmetrical signals of Fig. 2.21 indicate that the NL response of the samples is faster than 150 fs, the laser pulse duration. From these measurements, we determined $6.5 \times 10^{-16} < n_2 < 8.0 \times 10^{-16}$ cm^2/W. As for 1064 nm, the NL absorption coefficients of the samples were smaller than the minimum value that our apparatus could measure (0.003 cm/GW). The results are summarized in Table 2.2.

It is important to note that the values of α_2 for both wavelengths are at least one order of magnitude smaller than the results reported for other TeO_2-based glasses. Then, with basis on the present measurements, we calculated the figures of merit for all-optical switching, $F = n_2/\lambda\alpha_2$, and we obtained $F > 1$ for all samples that indicate the possibility of using the materials for all-optical switching [67].

2.5 Conclusion

In this chapter, the frequency upconversion PL properties and the NL optical response of some tellurium oxide glasses were reviewed. Enhancement of the PL properties due to the contribution of phonon-assisted transitions in neodymium-

doped glasses or due to the presence of silver or silicon NPs in samples singly- and co-doped with different rare-earth ions (terbium, thulium, erbium, europium, and ytterbium) was described, for light excitation in the visible and in the near-infrared. Energy transfer from excited silver NPs to the rare-earth ions and growth of the local electromagnetic field due to difference between the dielectric function of the NPs and the host material are the mechanisms contributing for PL enhancements that in some cases reach more than one order of magnitude. In the samples with silicon NPs, the mechanism contributing for the increase in the PL efficiency is the energy transfer from excited silicon NPs to the ions that are promoted from the ground state to excited states from where they emit light in the visible and in the infrared. Measurements of the NL refractive index and NL absorption coefficients for tellurium oxide glasses containing bismuth oxide in their compositions were also reviewed. The experiments discussed demonstrate that the NL parameters in the near-infrared are equally influenced by the TeO_2 and Bi_2O_3 components present in the samples. The glasses studied exhibit large NL refractive indices, but small NL absorption coefficients and their values indicate the possibility of using the samples for all-optical switching devices at the near-infrared in the sub-picosecond regime.

In conclusion, the works reviewed here demonstrated the large potential of new tellurium oxide glass compositions for luminescent devices and ultrafast all-optical switching.

Acknowledgments We acknowledge financial support from the Brazilian Agencies: Conselho Nacional de Desenvolvimento Científico e Tecnológico (CNPq) and Fundação de Amparo à Ciência e Tecnologia do Estado de Pernambuco (FACEPE). The work reported here was performed in the framework of the National Institute of Photonics (INCT de Fotônica) and PRONEX-CNPq/FACEPE projects. We acknowledge the Nanotechnology National Laboratory (LNNano), CNPEM Campinas, Brazil, and Laboratório de Microscopia Eletrônica/IFUSP for TEM measurements.

References

1. R.A.H. El-Mallawany, *Tellurite Glass Handbook: Physical Properties and Data* (CRC, Boca Raton, FL, 2001)
2. NIIR Board of Consultants and Engineers, *The Complete Book on Glass and Ceramics Technology* (Asia Pacific Business Press, Inc., India, 2005)
3. A. Margaryan, M. A. Piliavin (eds.), *Germanate Glasses: Structure, Spectroscopy and Properties* (Artech House Inc., Boston, 1993)
4. M. Razeghi (ed.), *Antimony: Characteristics, Compounds and Applications* (Nova Science Publishers, New York, 2012)
5. M. Yamane, Y. Asahara, *Glasses for Photonics* (Cambridge University Press, Cambridge, 2000)
6. L.R.P. Kassab, C.B. de Araújo, in *Photonics Research Development*, ed. by V.P. Nilsson (Nova Science Publishers, Inc., New York, 2008)
7. K. Fedus, G. Boudebs, Opt. Commun. **292**, 140 (2013)
8. K. Fedus, G. Boudebs, Opt. Commun. **284**, 1057 (2011)

9. R.J. Sutherland, *Handbook of Nonlinear Optics* (Wiley, New York, 1996)
10. R. Scheps, Prog. Quantum Electron. **20**, 271 (1996)
11. H.-Q. Wang, M. Batentschuk, A. Osvet, L. Pinna, C.J. Brabec, Adv. Mater. **23**, 2675 (2011)
12. G.S. Maciel, L.d.S. Menezes, A.S.L. Gomes, C.B. de Araújo, Y. Messaddeq, A. Florez, M.A. Aegerter, IEEE Photonics Technol. Lett. **7**, 1474 (1995)
13. E. Downing, L. Hesselink, J. Ralston, R. Macfarlane, Science **273**, 1185 (1996)
14. M.S. Marques, L.d.S. Menezes, W. Lozano B., L.R.P. Kassab, C.B. de Araújo, J. Appl. Phys. **113**, 053102 (2013)
15. F. Auzel, Phys. Rev. B **13**, 2809 (1976)
16. L.d.S. Menezes, G.S. Maciel, C.B. de Araújo, Y. Messaddeq, J. Appl. Phys. **90**, 4498 (2001)
17. O.L. Malta, P.A.S. Cruz, G.F. de Sá, F. Auzel, JOL **33**, 261 (1985)
18. A. Pillonnet, A. Berthelot, A. Pereira, O. Benamara, S. Derom, G.C. des Francs, A.M. Jurdyc, Appl. Phys. Lett. **100**, 153115 (2012)
19. T. Hayakawa, S.T. Selvan, M. Nogami, Appl. Phys. Lett. **74**, 1513 (1999)
20. L.P. Naranjo, C.B. de Araújo, O.L. Malta, P.A.S. Cruz, L.R.P. Kassab, Appl. Phys. Lett. **87**, 24194 (2005)
21. V.K. Rai, L.d.S. Menezes, C.B. de Araújo, L.R.P. Kassab, D.M. da Silva, R.A. Kobayashi, J. Appl. Phys. **103**, 093526 (2008)
22. L.R.P. Kassab, D.S. da Silva, R. de Almeida, C.B. de Araújo, Appl. Phys. Lett. **94**, 101912 (2009)
23. T. Som, B. Karmakar, J. Appl. Phys. **105**, 013102 (2009)
24. V.A.G. Rivera, S.P.A. Osorio, Y. Ledemi, D. Manzani, Y. Messaddeq, L.A.O. Nunes, E. Marega Jr., Opt. Express **18**, 25321 (2010)
25. R.J. Amjad, M.R. Sahar, M.R. Dousti, S.K. Ghoshal, M.N.A. Jamaludin, Opt. Express **21**, 14282 (2013)
26. L.R.P. Kassab, L.F. Freitas, T.A.A. Assumpção, D.M. da Silva, C.B. de Araújo, Appl. Phys. B **104**, 1029 (2011)
27. C.B. de Araújo, D.S. da Silva, T.A.A. de Assumpção, L.R.P. Kassab, D.M. da Silva, Sci. World J. **2013**, 385193 (2013)
28. C.B. de Araújo, L.R.P. Kassab, R.A. Kobayashi, L.P. Naranjo, P.A.S. Cruz, J. Appl. Phys. **99**, 123522 (2006)
29. L.R.P. Kassab, C.B. de Araújo, R.A. Kobayashi, R.d.A. Pinto, D.M. da Silva, J. Appl. Phys. **102**, 103515 (2007)
30. R. de Almeida, D.M. da Silva, L.R.P. Kassab, C.B. de Araújo, Opt. Commun. **281**, 108 (2008)
31. L.R.P. Kassab, R. de Almeida, D.M. da Silva, C.B. de Araújo, J. Appl. Phys. **104**, 093531 (2008)
32. L.R.P. Kassab, R. de Almeida, D.M. da Silva, T.A.A. de Assumpção, C.B. de Araújo, J. Appl. Phys. **105**, 103505 (2009)
33. T.A.A. de Assumpção, D.M. da Silva, M.E. Camilo, L.R.P. Kassab, A.S.L. Gomes, C.B. de Araújo, N.U. Weter, J. Alloys Compd. **586**, S516 (2014)
34. V.P.P. de Campos, L.R.P. Kassab, T.A.A. de Assumpção, D.S. da Silva, C.B. de Araújo, J. Appl. Phys. **112**, 063519 (2012)
35. D.S. da Silva, T.A.A. de Assumpção, G.B.C. de Simone, L.R.P. Kassab, C.B. de Araújo, Appl. Phys. B **121**, 117 (2015)
36. L. Yu, H. Liu, J. Nanomater. **2010**, 461309 (2010)
37. G. Wang, W. Qin, L. Wang, G. Wei, P. Zhu, R. Kim, Opt. Express **16**, 11907 (2008)
38. R.H. Page, K.I. Schaffers, P.A. Waide, J.B. Tassano, S.A. Payne, W.F. Krupke, W.K. Bischel, J. Opt. Soc. Am. B **15**, 996 (1998)
39. T.A.A. Assumpção, D.M. da Silva, L.R.P. da Silva, C.B. de Araújo, J. Appl. Phys. **106**, 063522 (2009)
40. P.B. Johnson, R.W. Christy, Phys. Rev. B **6**, 4370 (1972)
41. D.M. da Silva, L.R.P. Kassab, S.R. Luthi, C.B. de Araújo, A.S.L. Gomes, M.J.V. Bell, Appl. Phys. Lett. **90**, 081913 (2007)

42. A.A. Bol, R. van Beek, A. Meijerink, Chem. Mater. **14**, 1121 (2002)
43. D.J. Lockwood, J. Mater. Sci. Mater. Electron. **20**, S235 (2009)
44. M.J.A. de Dood, J. Knoester, A. Tip, A. Polman, Phys. Rev. B **71**, 115102 (2005)
45. X.L. Wu, Y.F. Mei, G.G. Siu, K.L. Wong, K. Moulding, M.J. Stokes, C.L. Fu, X.M. Bao, Phys. Rev. Lett. **86**, 3000 (2001)
46. R.A. Senter, C. Pantea, Y. Wang, H. Liu, T.W. Zerda, J.L. Coffer, Phys. Rev. Lett. **93**, 175502 (2004)
47. E.F. Pecora, T.I. Murphy, L.D. Negro, Appl. Phys. Lett. **101**, 191115 (2012)
48. N. Koshida (ed.), *Device Applications of Silicon Nanocrystals and Nanostructures*. Nanostructure Science and Technology (Springer, New York, 2009)
49. A.J. Kenyon, Prog. Quantum Electron. **26**, 225 (2002)
50. F. Priolo, G. Franzò, D. Pacifici, V. Vinciguerra, F. Iacona, A. Irrera, J. Appl. Phys. **89**, 264 (2001)
51. A. Irrera, F. Iacona, G. Franzò, M. Miritello, R.L. Savio, M.E. Castagna, S. Coffa, F. Priolo, J. Appl. Phys. **107**, 054302 (2010)
52. C. Meier, A. Gondorf, S. Lüttjohann, A. Lorke, H. Wiggers, J. Appl. Phys. **101**, 103112 (2007)
53. C. Delarue, G. Allan, M. Lannoo, Phys. Rev. B **48**, 11024 (1993)
54. D.S. da Silva, L.P. Naranjo, L.R.P. Kassab, C.B. de Araújo, Appl. Phys. B **106**, 1015 (2012)
55. Y. Chen, Q. Nie, T. Xu, S. Dai, X. Wang, X. Shen, J. Non Cryst. Solids **354**, 3468 (2008)
56. V.K. Rai, L.d.S. Menezes, C.B. de Araújo, Appl. Phys. A **91**, 441 (2008)
57. E. Yousef, M. Hotzel, C. Rüssel, J. Non Cryst. Solids **342**, 82 (2004)
58. E. Yousef, M. Hotzel, C. Rüssel, J. Non Cryst. Solids **353**, 333 (2007)
59. L. Canioni, M.O. Martin, B. Bousquet, L. Sarger, Opt. Commun. **151**, 241 (1998)
60. S. Kim, T. Yoko, J. Am. Ceram. Soc. **78**, 1061 (1995)
61. H. Nasu, T. Uchigaki, K. Kamiya, H. Kanbara, Jpn. J. Appl. Phys. **31**, 3899 (1992)
62. M. Lines, Phys. Rev. B **43**, 11978 (1991)
63. A.P. Mirgorodsky, M. Soulis, P. Thomas, T. Merle-Méjean, M. Smirnov, Phys. Rev. B **73**, 134206 (2006)
64. T.A. Oliveira, D. Manzani, E.L. Falcão-Filho, Y. Messaddeq, G. Boudebs, K. Fedus, C.B. de Araújo, Appl. Phys. B **116**, 1 (2014)
65. D. Manzani, J.L. Ferrari, F.C. Polachini, Y. Messaddeq, S.J.L. Ribeiro, J. Mater. Chem. **22**, 16540 (2012)
66. D. Manzani, Y. Ledemi, I. Skripachev, Y. Messaddeq, S.J.L. Ribeiro, R.E.P. de Oliveira, C.J.S. de Matos, Opt. Mater. Express **1**, 1515 (2011)
67. G.I. Stegeman, in *Nonlinear Optics of Organic Molecules and Polymers*, ed. by H.S. Nalva, S. Miyata (CRC, Boca Raton, FL, 1997), p. 799

Springer

http://www.springer.com/978-3-319-53036-9

Technological Advances in Tellurite Glasses
Properties, Processing, and Applications
Rivera, V.A.G.; Manzani, D. (Eds.)
2017, IX, 335 p. 169 illus., 117 illus. in color., Hardcover
ISBN: 978-3-319-53036-9